EDGE ARTICLE

A *Λ*-Ir(III)-phenylquinazolinone complex enhances ferroptosis by selectively inhibiting metallothionein-1†

Lu Zhu,[a] Xingyun Wang,[a] Tian Tian,[b] Yanyan Chen,[b] Wenjing Du,[b] Wei Wei,*[abc] Jing Zhao, [iD] *[bc] Zijian Guo [iD] [b] and Xiuxiu Wang*[b]

Chirality plays an indispensable role in various biological processes, and interactions between chiral enantiomers and biomolecular targets provide new perspectives in precision drug development. While ferroptosis has received increasing attention as a novel pathway to reverse drug resistance, work on the design of precise ferroptosis-targeting molecules through chiral programming was limited. In this work, we designed and synthesized a pair of chirality-dependent ferroptosis-inducing Ir(III)-phenylquinazolinone complexes (*Δ*-**IrPPQ** and *Λ*-**IrPPQ**) by inhibiting ferroptosis suppressor protein-1 (FSP1), while the pair of **IrPPQ** complexes induced extremely different ferroptosis effects as well as distinct photodynamic therapy (PDT) responses toward pancreatic cancer cells. Interestingly, this chirality-dependent biological mechanism through proteomic analysis and molecular simulation revealed that the specific binding and inhibition of metallothionein-1 (MT1) by *Λ*-**IrPPQ** sensitized cancer cells to ferroptosis, inducing a burst of reactive oxygen species, lipid peroxidation, glutathione depletion, and inactivation of FSP1. While in comparison, *Δ*-**IrPPQ** induced mild ferroptotic cell death. Through simple chiral resolution, the obtained *Λ*-**IrPPQ** achieved precise regulation of ferroptosis in pancreatic cancer cells. This work provides new insights into the design of chiral ferroptosis-inducing metallodrugs for future pancreatic cancer therapy.

Introduction

Chirality is one of the essential features of life entities and plays an important role in the development of new drugs. Two mirror isomers of chiral drugs can have dramatically different biological responses, such as toxicity and pharmacokinetics.[1] Metal coordination is one of the most powerful approaches for chiral chemical transformations,[2] and chiral metallodrugs with metal-centered or carbon-centered chirality have attracted increasing attention due to the outstanding chiral-specific recognition of biomacromolecules in cancer therapy.[3–5] For example, pioneering work by Qu *et al.* designed chiral metallo-supramolecular complexes to enantioselectively bind with G-quadruplex DNA to induce apoptosis of breast cancer stem cells,[6] and a recent report on chiral AuNPs by Xu *et al.* showed that enantioselective binding with adhesion G-protein-coupled

receptors regulated the maturation of immunological dendritic cells.[7] Chiral resolution and precise synthesis of chiral drugs provide powerful tools for the specific recognition of macromolecules in cancer cells. However, the acquired or intrinsic resistance of cancer cells to apoptosis is prone to occur during preclinical and clinical cancer chemotherapy or phototherapy, leading to the emergence of drug resistance in clinical practice.[8,9] To reverse the apoptosis resistance of metallodrugs, a rational design of metallodrugs with precise chirality for specific recognition of target proteins to induce non-apoptotic pathways is urgently needed.

Ferroptosis, a newly discovered iron-dependent non-apoptotic form of programmed cell death, plays a pivotal role in cancer therapy and has been shown to reverse drug resistance of apoptosis-resistant cancer cells.[10–15] Induction of cell ferroptosis led to the effective anticancer proliferation activities toward multiple types of cancer.[16,17] In particular, for pancreatic ductal adenocarcinoma (PDAC), a ferroptosis-sensitive cell line, deletion of *Slc7a11* by ferroptosis inducers resulted in excellent inhibition of PDAC in mice.[18] Recently, the development of metal complexes (Ir(III),[19–26] Fe(III),[27–31] and Ga(III)[32–34]) by inducing ferroptosis has shown significant advantages in disrupting Fe metabolism, glutathione metabolism and regulating immune responses. In addition, targeting ferroptosis suppressor protein-1 (FSP1, a glutathione-independent

[a]School of Life Sciences, Nanjing University, Nanjing, 210023, China. E-mail: weiwei@nju.edu.cn; jingzhao@nju.edu.cn; wangxiuxiu@nju.edu.cn

[b]Chemistry and Biomedicine Innovation Center (ChemBIC), State Key Laboratory of Coordination Chemistry, School of Chemistry and Chemical Engineering, Nanjing University, Nanjing, 210023, China

[c]Nanchuang (Jiangsu) Institute of Chemistry and Health, Sino-Danish Ecolife Science Industrial Incubator, Jiangbei New Area, Nanjing, 210000, China
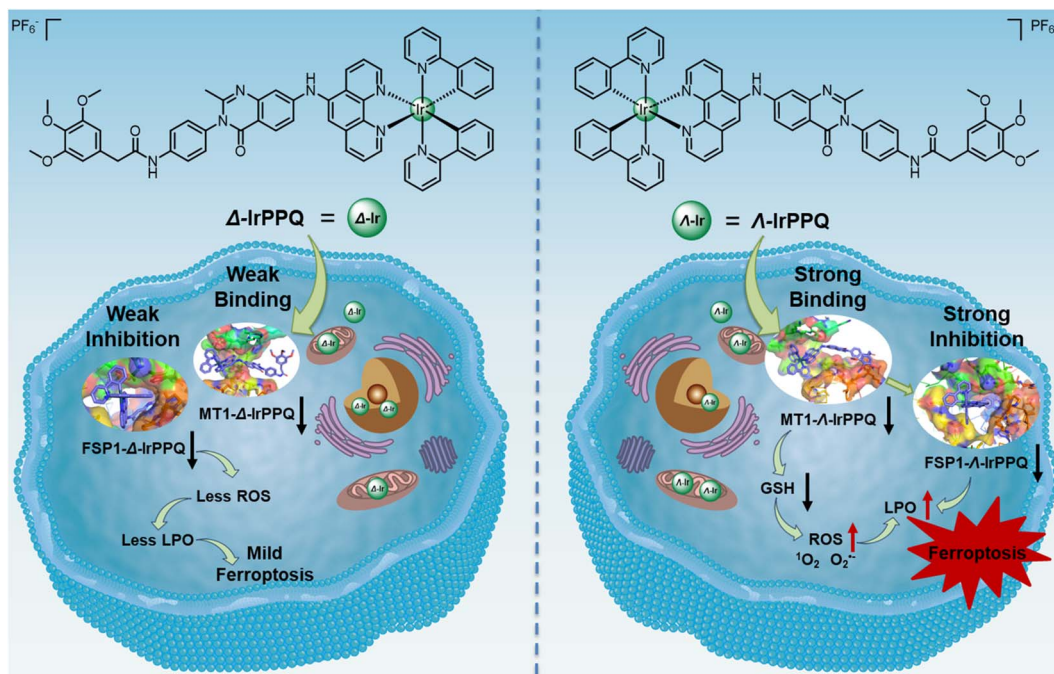
Scheme 1 Schematic illustration of two chiral Ir(III) complexes (*Δ*-IrPPQ and *Λ*-IrPPQ) in inducing chirality-dependent ferroptosis through specific recognition and binding with metallothionein-1 (MT1).

ferroptosis suppressor) by an AIE-based Pt(II) complex induced ferroptosis with potential to overcome drug resistance.[35] However, little effort has been devoted to the design and exploration of metal chirality in the regulation of ferroptosis.

Here, we designed and synthesized a pair of enantiomeric iridium(III) complexes (*Δ*-IrPPQ and *Λ*-IrPPQ) with phenylquinazolinone-derived ancillary ligand to target FSP1 and induce ferroptosis. *Δ*-IrPPQ and *Λ*-IrPPQ were well characterized by ^{1}H NMR, ^{13}C NMR and HR-ESI-MS, and the photophysical properties of *Δ*-IrPPQ and *Λ*-IrPPQ were investigated by UV-vis absorption, fluorescence and circular dichroism (CD) spectroscopies. Interestingly, the pair of **IrPPQ** complexes induced extremely different ferroptosis effects as well as different photodynamic therapy (PDT) responses towards pancreatic cancer cells. This chirality-dependent ferroptosis-inducing mechanism was investigated in detail by proteomic analysis and molecular simulation (Scheme 1).

Results and discussion

Design, synthesis, and characterization of chiral iridium(III) complexes

As a targeting molecule of ferroptosis suppressor protein-1 (FSP1), the reported 3-phenylquinazolinone has been confirmed to precisely bind to FSP1 and induce ferroptotic cell death.[36–38] In this work, we designed a N^N ligand with phenylquinazolinone skeleton and introduced it into the chiral cyclometalated Ir(III) complexes to construct a pair of enantiopure Ir(III) complexes. As shown in Scheme 2, we first separated cyclometalated precursors *Δ*-Ir-*R* and *Λ*-Ir-*R* by simply introducing enantiopure ancillary ligand (*R*)-Fphox according to the

reported method.[39,40] The synthetic route of **PPQ** is detailed in ESI Scheme S1.† *Δ*-Ir-*R* and *Λ*-Ir-*R* subsequently coordinated with **PPQ** ligand to afford two enantiopure Ir(III) complexes *Δ*-IrPPQ and *Λ*-IrPPQ. To gain insight into 3D structures of *Δ*-IrPPQ and *Λ*-IrPPQ, geometry optimizations were performed by Gaussian optimization and the 3D structures were displayed in Scheme 2. Both of *Δ*-IrPPQ and *Λ*-IrPPQ were well characterized by NMR spectroscopy (^{1}H NMR and ^{13}C NMR, ESI Fig. S1–S9†) and high-resolution electrospray ionization mass spectrometry (HR-ESI-MS, Fig. 1a and ESI S10–S12†). HR-ESI-MS spectra of *Δ*-IrPPQ and *Λ*-IrPPQ show peaks at $m/z = 1153.3342$ and $m/z = 1153.3366$ respectively, corresponding to $[\text{M-PF}_6^-]^+$ species (Fig. 1a), which are in good agreement with their calculated theoretical values.
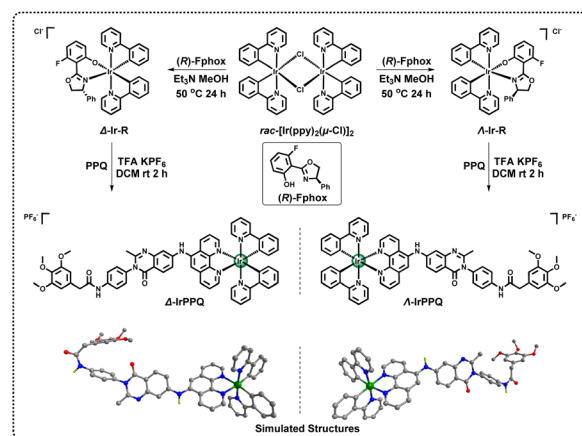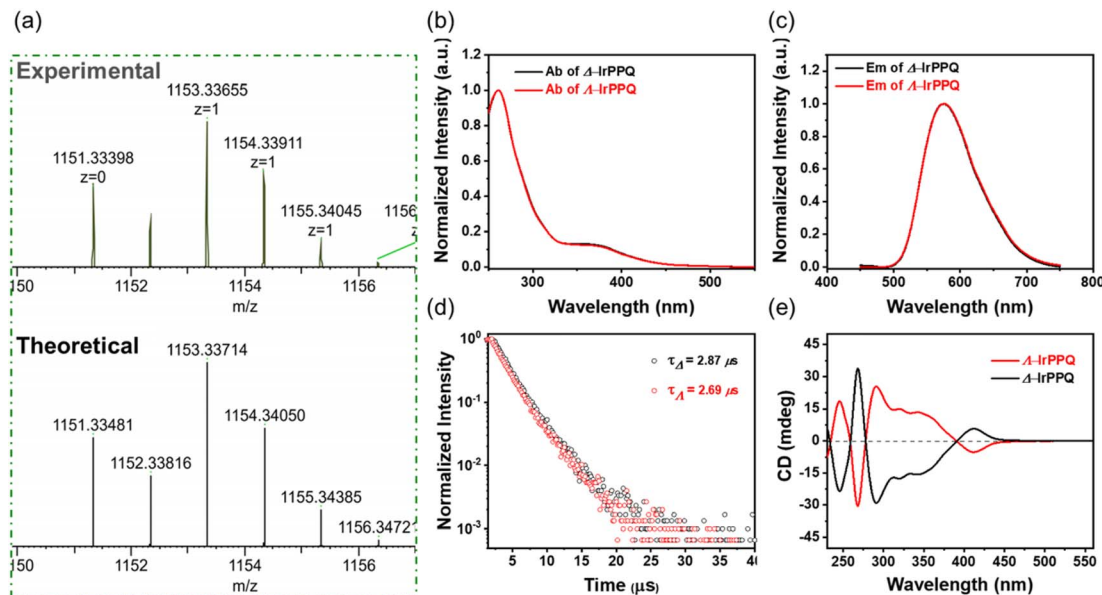

Scheme 2 Synthesis of *Δ*-IrPPQ and *Λ*-IrPPQ.

Fig. 1 (a) Experimental (green) and calculated (black) HR-ESI-MS spectra of Λ-IrPPQ. (b) UV-vis absorption spectra of Δ-IrPPQ and Λ-IrPPQ. (c) Photoluminescent spectra of Δ-IrPPQ and Λ-IrPPQ. (d) Transient decay curves of Δ-IrPPQ and Λ-IrPPQ. (e) CD spectra of Δ-IrPPQ and Λ-IrPPQ (dichloromethane, 2×10^{-5} M).

Photophysical properties of chiral iridium(III) complexes

The photophysical properties of Δ-IrPPQ and Λ-IrPPQ were investigated by UV-vis absorption spectra, photoluminescence (PL) spectra and circular dichroism (CD) spectra, and compared in Fig. 1b, c and e. The absorption and emission spectra measured in degassed dichloromethane (DCM, 2×10^{-5} M) are very similar. The absorption bands at around 260 and 370 nm can be attributed to the spin-allowed ligand-centered (LC) $^1\pi\pi^*$ transition and metal-to-ligand charge transfer (MLCT), respectively. Both Δ-IrPPQ and Λ-IrPPQ exhibited a broad emission spectrum centered at 575 nm in DCM solution. The emission lifetimes of Δ-IrPPQ and Λ-IrPPQ were measured at the peak wavelength in degassed DCM solution by single-exponential fitting of the decay curves, giving average lifetimes of 2.87 and 2.69 μs with photoluminescence quantum yields (PLQY) of 43.3 and 49.7%, respectively (Fig. 1d). The CD spectra of Δ-IrPPQ and Λ-IrPPQ showed a good mirror image relationship with alternating positive and negative Cotton effects from 230 to 450 nm, confirming the optical purity of two Ir(III) complexes. The strong CD signals below 390 nm can be attributed to the $^1\pi\pi^*$ transition of cyclometallic ligands, and the lower energy signal at 410 nm can be attributed to metal–ligand charge transfer (MLCT), corresponding to their absorption properties.

In vitro antiproliferation activities of chiral iridium(III) complexes

Based on the extensive investigations of metal-based drugs in the field of anticancer, the antiproliferative activities of PPQ ligand, Δ-IrPPQ, Λ-IrPPQ and rac-IrPPQ were evaluated in human fibrosarcoma HT-1080 cells, human malignant melanoma SK-MEL-28 cells and human pancreatic cancer PANC-1 cells in both dark and light conditions by using 3-(4,5-dimethylthiazol-2-yl)-2,5-diphenyltetrazolium bromide (MTT) assay and the IC_{50} values are listed in Tables 1 and ESI S1.† All tested compounds showed negligible cytotoxicity towards cancer cells in the dark, indicating the biocompatibility and biosafety of synthesized complexes. After exposure to light (380–390 nm, 30 mW cm^{-2}) for 10 min, the cytotoxicity of both Δ-IrPPQ and Λ-IrPPQ increased, while the photocytotoxicity of rac-IrPPQ was still relatively low ($IC_{50} > 50$ μM). More interestingly, Δ-IrPPQ and Λ-IrPPQ exhibited pronounced photocytotoxicity against the tested cancer cells, especially for PANC-1 cells. The cytotoxic $(IC_{50})_{irrad}$ value of Λ-IrPPQ was 2.70 μM, much lower than that of Δ-IrPPQ ($(IC_{50})_{irrad} > 50$ μM). And the corresponding photocytotoxicity index (PI) value of Λ-IrPPQ was 185.2, which was much higher than that of Δ-IrPPQ and rac-IrPPQ, demonstrating the enantiopure Λ-IrPPQ as a potential iridium PDT agent, especially for its superior biocompatibility under dark conditions and its high PI value. This chirality-dependent PDT effect was further confirmed by calcein AM/propidium iodide co-staining assay in PANC-1 cells (Fig. 2a). When compared to the first reported Iridium(III)-based ferroptosis inducer (IrFN),[19] Λ-IrPPQ also displayed higher cytotoxicity toward PANC-1 cells than IrFN (Table S2†). In addition, the photocytotoxicity index of Λ-IrPPQ was higher than most

Table 1 IC_{50} values of Δ-IrPPQ, Λ-IrPPQ and rac-IrPPQ toward PANC-1 cells in dark and light condition (Ex = 380–390 nm, 30 mW cm^{-2}, 10 min)

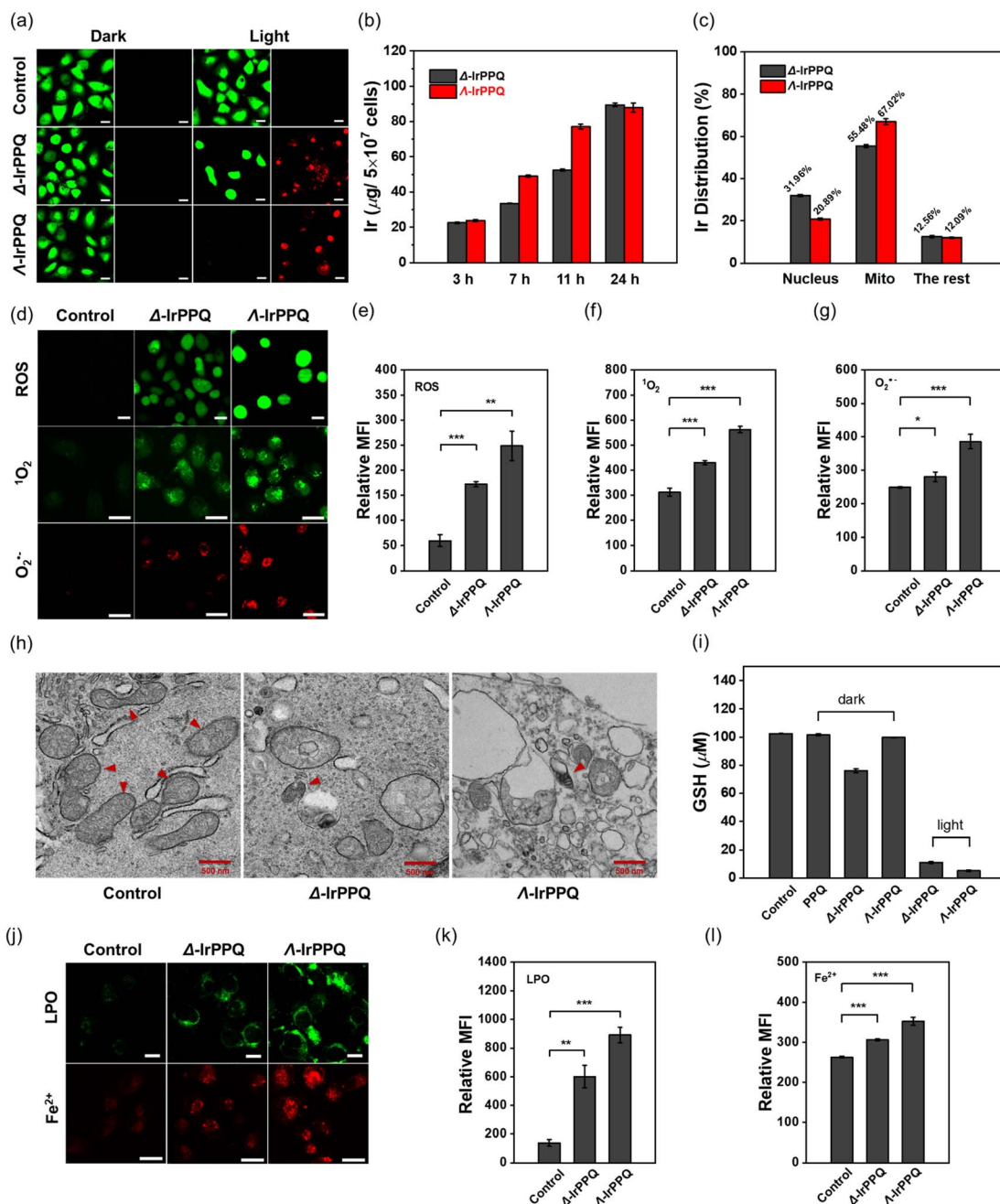| IC_{50} (μM)		Δ-IrPPQ	Λ-IrPPQ	rac-IrPPQ
PANC-1	Dark	>500	>500	>500
	Light	>50	2.70 ± 0.11	66.67 ± 1.19
	PI	<10	185.2	7.50

Fig. 2 (a) Imaging of 10 μM **Δ-IrPPQ** and **Λ-IrPPQ** treated PANC-1 cells in the dark or after irradiation *via* calcein AM/propidium iodide co-staining. Scale bar: 20 μm. (b) Cellular uptake of Ir in 10 μM **Δ-IrPPQ** and **Λ-IrPPQ** treated PANC-1 cells. (c) Subcellular distribution of **Δ-IrPPQ** and **Λ-IrPPQ** in PANC-1 cells. (d) Imaging of photoinduced ROS, $^1O_2$ and $O_2^{\bullet-}$ *via* DCFH-DA, SOSG and MitoSOX Red staining, respectively. Scale bar: 20 μm. (e) Relative mean fluorescence intensity (MFI) of ROS produced in cells treated with **Δ-IrPPQ** and **Λ-IrPPQ** after irradiation. (f) Relative mean fluorescence intensity (MFI) of $^1O_2$ produced in cells treated with **Δ-IrPPQ** and **Λ-IrPPQ** after irradiation. (g) Relative mean fluorescence intensity (MFI) of $O_2^{\bullet-}$ produced in cells treated with **Δ-IrPPQ** and **Λ-IrPPQ** after irradiation. (h) Morphology of mitochondria (indicated by red arrow) in PBS, **Δ-IrPPQ** and **Λ-IrPPQ** treated (10 μM) PANC-1 cells after irradiation *via* transmission electron microscope imaging. Scale bar: 500 nm. (i) Intracellular GSH levels in PBS, **PPQ**, **Δ-IrPPQ** and **Λ-IrPPQ** treated PANC-1 cells (10 μM, dark and light). (j) Imaging of intracellular lipid peroxides (LPO) and Fe^{2+} *via* BODIPY 581/591 C11 and FeRhoNox-1 staining, respectively. Scale bar: 20 μm. (k) Relative mean fluorescence intensity (MFI) of LPO in cells after treatments. (l) Relative mean fluorescence intensity (MFI) of Fe^{2+} in cells after treatments. All irradiation condition: 380–390 nm, 30 mW cm^{-2}, 10 min. Data are mean ± s.d. ($n = 3$). *$P < 0.05$, **$P < 0.01$, ***$P < 0.001$, analyzed by Student's t-test.

reported ferroptosis-inducing metal agents (Table S2†),[20–26,32–35] confirming the high cancer cell killing efficiency as a potential PDT agent.

Cellular uptake and distribution of chiral iridium(III) complexes

This difference in the photocytotoxicity of Δ-IrPPQ and Λ-IrPPQ against tested cancer cells encouraged us to investigate their cellular mechanism. Since the cellular uptake of metal is one of the key factors affecting the cytotoxicity of metal drugs, we first investigated the intracellular uptake of Δ-IrPPQ and Λ-IrPPQ in PANC-1 cells by inductively coupled plasma mass spectrometry (ICP-MS). As shown in Fig. 2b, the total iridium content in Δ-IrPPQ and Λ-IrPPQ treated PANC-1 cells increased with increasing incubation time, and the uptake of Λ-IrPPQ was significantly faster than that of Δ-IrPPQ within 24 h. In terms of biodistribution of the two enantiomers, Λ-IrPPQ showed a higher mitochondrial targeting ability (67.02%), whereas Δ-IrPPQ was more abundant in the nucleus (31.96%) (Fig. 2c). This discrepancy in subcellular biodistribution may dominate the different PDT effects and the chirality-dependent mechanism requires further investigation.

Chirality-dependent ferroptosis induced by Δ-IrPPQ and Λ-IrPPQ

Reactive oxygen species (ROS) play a critical role in the PDT process for cancer treatment, and intracellular photo-induced ROS was first evaluated in PANC-1 cells by DCFH-DA staining. As shown in Fig. 2d and e, a large amount of ROS was produced by Δ-IrPPQ and Λ-IrPPQ after photoirradiation, and an apparent fluorescence enhancement can be observed in Λ-IrPPQ treated cells. In addition, the types of reactive oxygen species induced by chiral IrPPQ complexes were also investigated by SOSG and MitoSOX red staining (Fig. 2d, f and g). Cellular imaging revealed that both $^1O_2$ and $O_2^{\cdot-}$ were generated in Δ-IrPPQ and Λ-IrPPQ treated PANC-1 cells after photoirradiation, whereas Λ-IrPPQ induced more $^1O_2$ and $O_2^{\cdot-}$ accumulation than Δ-IrPPQ. In terms of ROS production capacity, this discrepancy induced the corresponding chirality-dependent photocytotoxicity.

As complexes containing a 3-phenylquinazolinone skeleton, the ferroptosis-inducing capacity of two enantiomers was then investigated. We first evaluated the influence on ferroptosis-specific mitochondrial morphology. As displayed in Fig. 2h, the shrunken mitochondria and mitochondrial cristae collapse could be observed in both Δ-IrPPQ and Λ-IrPPQ treated cells when compared to the PBS group by transmission electron microscopy (TEM) imaging, indicating the ferroptotic cell death induced by two enantiomers. As one of the hallmarks of ferroptosis, intracellular GSH concentration was detected and we found that Δ-IrPPQ and Λ-IrPPQ caused a sharp decrease in total GSH, which weakened the antioxidant capacity of cells (Fig. 2i). The accumulation of lipid peroxides (LPO), which is produced by the oxidative attack of ROS on polyunsaturated fatty acids (PUFAs),[41] was also evaluated in Δ-IrPPQ and Λ-IrPPQ treated PANC-1 cells by BODIPY 581/591 C11 staining.

Confocal imaging revealed that intracellular lipid peroxides were increased 4.3-fold by Δ-IrPPQ treatment and 6.4-fold by Λ-IrPPQ treatment compared to the control group (Fig. 2j and k). Furthermore, a higher release of Fe^{2+} can be observed in Λ-IrPPQ treated cells by FeRhoNox-1 staining (Fig. 2j and l). Taken together, the more obvious ROS production, GSH depletion, lipid ROS accumulation and Fe^{2+} release in Λ-IrPPQ treated cells indicated that Λ-IrPPQ induced more significant ferroptotic cell death than Δ-IrPPQ.

Proteomic analysis of Δ-IrPPQ and Λ-IrPPQ in PANC-1 cells and validation of targeted proteins

To further elucidate the mechanism of the chirality-dependent ferroptosis effect induced by Δ-IrPPQ and Λ-IrPPQ, we then performed mass spectrometry-based proteomics analysis. By comparing the total protein changes of Δ-IrPPQ and Λ-IrPPQ with PBS groups, we found that 25 proteins were significantly downregulated and 4 proteins were significantly upregulated in Δ-IrPPQ treated cells (Fig. 3a). For Λ-IrPPQ treated cells, 25 proteins were significantly downregulated and 8 proteins were significantly upregulated (Fig. 3b). The expression of zinc finger and BTB domain-containing protein 40 (ZBTB40) was significantly inhibited in both Δ-IrPPQ and Λ-IrPPQ treated cells, while metallothionein-1X (MT1) was significantly downregulated only in Λ-IrPPQ treated cells (Fig. 3a and b). Then, by comparing the proteome of Δ-IrPPQ and Λ-IrPPQ treated cells, MT1, tubulin polymerization-promoting protein (TPPP), 5′-AMP-activated protein kinase subunit beta-1 (PRKAB1) were downregulated in Λ-IrPPQ treated cells (Fig. 3c). From the KEGG pathway analysis, ribosome, aminoacyl-tRNA biosynthesis, cysteine and methionine metabolism, endocytosis and nucleocytoplasmic transport pathways were significantly inhibited in both Δ-IrPPQ and Λ-IrPPQ treated cells, while RIG-I-like receptor signaling pathway, ErbB signaling pathway and PD-1 checkpoint signaling pathway were significantly inhibited by Λ-IrPPQ (Fig. 3d and e). Comparing Δ-IrPPQ with Λ-IrPPQ by KEGG analysis, the effects on complement and coagulation cascades, ECM-receptor interaction, spliceosome and proteoglycans in cancer pathways were significantly different (Fig. 3f). Furthermore, bioinformatics analysis of gene ontology (GO) enrichment revealed that Δ-IrPPQ and Λ-IrPPQ exerted different effects on biological processes such as negative regulation of fibrinolysis, negative regulation of blood coagulation, extracellular matrix organization and cell migration (Fig. 3g). By GO analysis, activity-regulated cytoskeleton-associated protein (ARC), WAP, Kazal, immunoglobulin, Kunitz and NTR domain-containing protein 1 (WFIKKN1), PRKAB1, MT1, E3 SUMO protein ligase (ZNF451) and TPPP were significantly downregulated in cells with Λ-IrPPQ treatment compared to Δ-IrPPQ (Fig. 3h). All these pathways and biological processes screened by proteomic analysis revealed the detailed intracellular changes treated by two chiral IrPPQ complexes. In particular, metallothionein-1, a distinct protein that was downregulated only in Λ-IrPPQ treated cells, might be the key regulator of ferroptosis sensitivity induced by two chiral IrPPQ complexes.
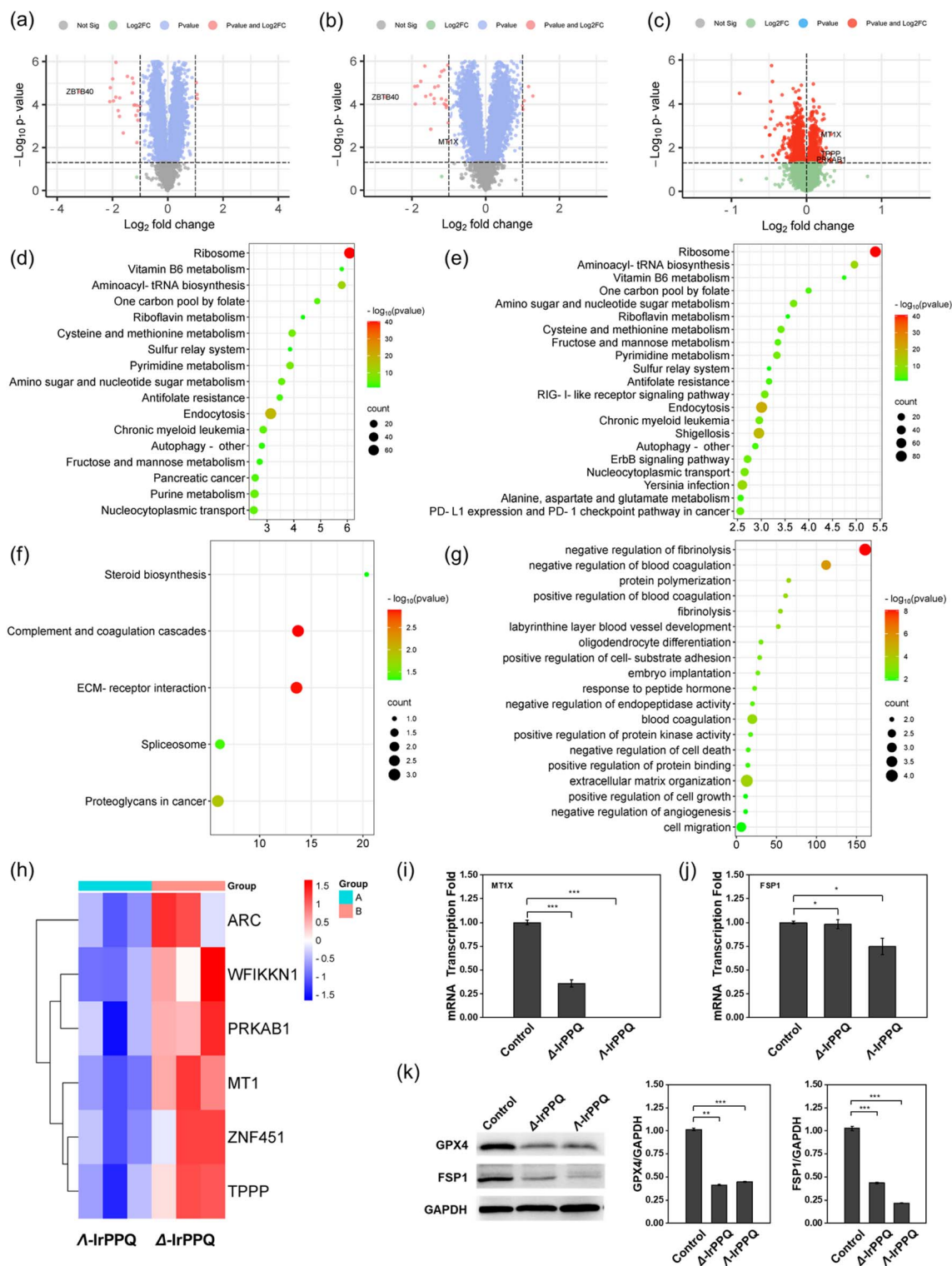
Fig. 3 Proteomic analysis of Δ-IrPPQ and Λ-IrPPQ in PANC-1 cells after light irradiation (380–390 nm, 30 mW cm^{-2}, 10 min). (a) Volcano plot of differentially expressed proteins in Δ-IrPPQ treated cells compared with PBS treated cells. (b) Volcano plot of differentially expressed proteins in Λ-IrPPQ treated cells compared with PBS treated cells. (c) Volcano plot of differentially expressed proteins in Δ-IrPPQ treated cells compared with Λ-IrPPQ treated cells. (d) KEGG pathway analysis of downregulated proteins in Δ-IrPPQ treated cells compared with PBS treated cells. (e) KEGG pathway analysis of downregulated proteins in Λ-IrPPQ treated cells compared with PBS treated cells. (f) KEGG pathway analysis of significantly differentially expressed proteins compared between Δ-IrPPQ and Λ-IrPPQ treated cells. (g) GO enrichment analysis of significantly differentially expressed proteins compared between Δ-IrPPQ and Λ-IrPPQ treated cells. (h) Heatmap of selected significantly differentially expressed proteins by GO analysis. (i) mRNA expression of MT1X in PBS, 10 μM Δ-IrPPQ and Λ-IrPPQ treated cells. (j) mRNA expression of FSP1 in PBS, 10 μM Δ-IrPPQ and Λ-IrPPQ treated cells. (k) Expression of GPX4 and FSP1 in PBS, 10 μM Δ-IrPPQ and Λ-IrPPQ treated cells by western blot analysis. Data are mean ± s.d. (n = 3). *$P < 0.05$, **$P < 0.01$, ***$P < 0.001$, analyzed by Student's t-test.
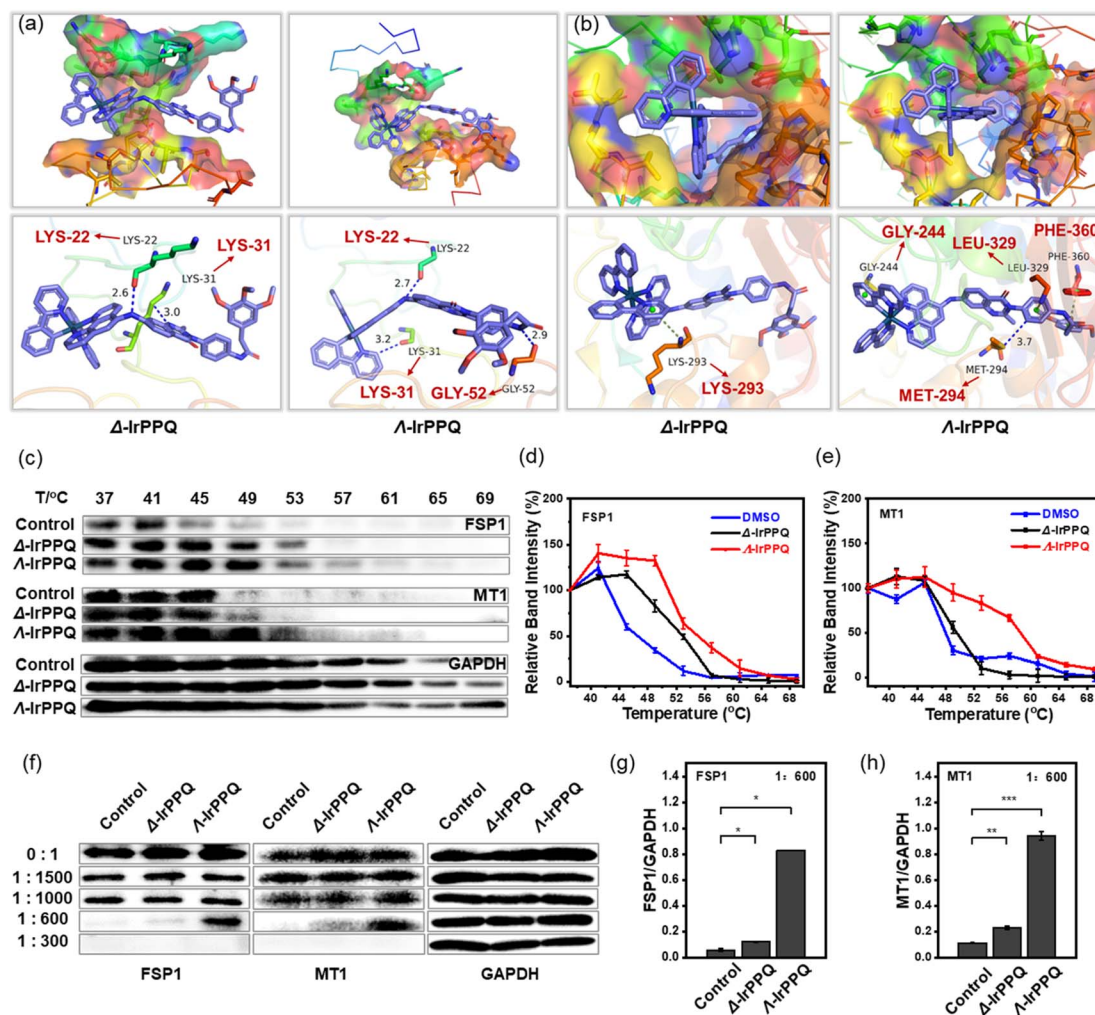
Fig. 4 (a) Molecular docking simulation studies investigating the binding modes of **Δ-IrPPQ** and **Λ-IrPPQ** with MT1. (b) Molecular docking simulation studies investigating the binding modes of **Δ-IrPPQ** and **Λ-IrPPQ** with FSP1. (c) Expression of FSP1 and MT1 in lysate of PANC-1 cells treated with DMSO (1%, v/v), 100 μM **Δ-IrPPQ** and 100 μM **Λ-IrPPQ** at different temperature gradients by western blot analysis. (d) CETSA curves of FSP1 treated with DMSO (1%, v/v), 100 μM **Δ-IrPPQ** and 100 μM **Λ-IrPPQ**. (e) CESTA curves of MT1 treated with DMSO (1%, v/v), 100 μM **Δ-IrPPQ** and 100 μM **Λ-IrPPQ**. (f) DARTS of FSP1 and MT1 in lysate of PANC-1 cells treated with DMSO (1%, v/v), 100 μM **Δ-IrPPQ** and 100 μM **Λ-IrPPQ** followed by different concentrations of pronase E (pronase E: total protein, w/w) by western blot analysis. (g) Quantification of FSP1 expression with treatments. (h) Quantification of MT1 expression with treatments.

As reported, upregulation of MT1 negatively regulates ferroptosis in clear cell renal cell carcinoma by reducing glutathione consumption,[42] and facilitates resistance to sorafenib-induced ferroptosis by altering redox metabolism in hepatocellular carcinoma cells.[43,44] Inhibition of MT1 induced ROS accumulation, lipid peroxidation, glutathione depletion and inactivation of FSP1, which sensitized cancer cells to ferroptosis.[43] In this work, the more significant inhibition of MT1 may confer greater sensitivity to ferroptosis in **Λ-IrPPQ** treated PANC-1 cells (Fig. 3i).

To confirm this ferroptosis sensitivity induced by **Λ-IrPPQ** by inhibiting MT1, we then detected the inhibition of FSP1 in cells treated with two chiral **IrPPQ** complexes. As shown in Fig. 3j and k, a significant inhibition of FSP1 was observed in **Λ-IrPPQ** treated cells by western blot and RT-qPCR analysis compared to **Δ-IrPPQ** treated group. No obvious difference can be observed in the inhibition of glutathione peroxidase 4 (GPX4), another

key regulator of ferroptosis. Therefore, in this work, the stronger inhibition of MT1 by **Λ-IrPPQ** promoted pancreatic cancer cells to be more sensitive to ferroptosis, and this sensitivity was originated from the enhanced inactivation of FSP1.

Molecular mechanism of the chirality-dependent protein binding

To further elucidate the molecular mechanism of this chirality-dependent inhibition of MT1 and FSP1 in ferroptosis, we then performed a molecular simulation analysis to investigate the binding mode of **Δ-IrPPQ** and **Λ-IrPPQ** with MT1 and FSP1. Through molecular docking calculation, **Λ-IrPPQ** was better integrated into the active pockets of MT1 and FSP1 with higher binding energies than **Δ-IrPPQ** (ESI Table S3†). As shown in Fig. 4a, two hydrogen bonds can form between **Δ-IrPPQ** and residues LYS22 and LYS31 of MT1, while three hydrogen bonds

can form between Λ-**IrPPQ** and MT1 at residues LYS22, GLY52 and LYS31. For FSP1, in addition to the π–π interaction between the phenyl moieties of Λ-**IrPPQ** and GLY244, PHE360 of FSP1, a hydrogen bond can also form in Λ-**IrPPQ** with residue LEU329 of FSP1. On the other hand, only a π–π interaction can be found in the pyridinyl moiety of Δ-**IrPPQ** with LYS293 of FSP1 and no hydrogen bond can be observed (Fig. 4b). From a molecular structural point of view, the chirality-dependent ferroptosis-inducing ability of Λ-**IrPPQ** during the PDT process was due to the specific binding of Λ-**IrPPQ** with MT1 and FSP1. These precise 3D configurations of Λ-**IrPPQ** with MT1 and FSP1 will provide new insights into the design of chiral metallodrugs to induce ferroptosis.

To further confirm the specific interaction of enantiomers with MT1 and FSP1, we investigated the stability of these two proteins with treatments. As the stability of small molecule-targeted proteins can be obviously enhanced in bioactive small molecule-treated protein pool,[45,46] the cellular thermal shift assay (CETSA) and drug affinity responsive target stability (DARTS) experiments on the detection of MT1 and FSP1 were then performed. As shown in Fig. 4c–e, the expression of MT1 and FSP1 in all groups decreased significantly with increasing temperature, while Λ-**IrPPQ** treated group showed the largest thermal shift for MT1 and FSP1 when compared to Δ-**IrPPQ** and control groups, revealing the more specific binding of Λ-**IrPPQ** with MT1 and FSP1. In addition, MT1 and FSP1 also exhibited stronger resistance to proteolysis in Λ-**IrPPQ** treated group (Fig. 4f–h). All these results confirmed the more specific binding of Λ-**IrPPQ** to MT1 and FSP1 than Δ-**IrPPQ**, which endowed Λ-**IrPPQ** with the chirality-dependent ferroptosis-inducing ability during PDT process.

Conclusions

In summary, we designed and synthesized the first case of chirality-dependent ferroptosis-inducing Ir(III) complexes (Δ-**IrPPQ** and Λ-**IrPPQ**) by enantioselectively inhibiting MT1 and FSP1. Δ-**IrPPQ** and Λ-**IrPPQ** induced distinct antitumor responses in PANC-1 cells after irradiation, and Λ-**IrPPQ** was able to induce more intracellular ROS, more GSH consumption, accumulation of lipid ROS and excessive release of Fe^{2+} in PANC-1 cells, indicating a stronger ferroptosis-inducing ability. Proteomic analysis screened out MT1 as a key regulator in this chirality-dependent ferroptosis process. Further molecular simulation analysis, CETSA and DARTS experiments confirmed that the specific binding of Λ-**IrPPQ** to MT1 dominated the enhanced sensitivity of pancreatic cancer cells to ferroptosis. In this work, through simple and effective chiral resolution, we obtained an enantiopure Ir(III) complex Λ-**IrPPQ** to precisely regulate the ferroptosis process and reverse the troublesome apoptosis resistance of pancreatic cancer cells, which opens a new avenue for the design of ferroptosis-inducing metallodrugs in future pancreatic cancer therapy via chiral programming.

Data availability

The data that support the findings of this study are available in the ESI† or on request from the corresponding author.

Author contributions

Dr Xiuxiu Wang, Jing Zhao, Wei Wei and Lu Zhu conceived and designed the study. Lu Zhu and Wenjing Du carried out the synthesis. Lu Zhu, Xingyun Wang, Tian Tian and Yanyan Chen performed the biological experiments. Lu Zhu, Xiuxiu Wang, Wei Wei, and Jing Zhao wrote the manuscript. All authors reviewed, provided suggestions, and approved the final version.

Conflicts of interest

The authors declare no conflict of interest.

Acknowledgements

Notes and references

1 J. H. Kim and A. R. Scialli, *Toxicol. Sci.*, 2011, **122**, 1–6.

2 Y. Wang, H. Huang, Q. Zhang and P. Zhang, *Dalton Trans.*, 2018, **47**, 4017–4026.

3 G. E. Atilla-Gokcumen, D. S. Williams, H. Bregman, N. Pagano and E. Meggers, *Chembiochem*, 2006, **7**, 1443–1450.

4 P. Goebel, F. Ritterbusch, M. Helms, M. Bischof, K. Harms, M. Jung and E. Meggers, *Eur. J. Inorg. Chem.*, 2015, (10), 1654–1659.

5 J. Debreczeni, A. N. Bullock, G. E. Atilla, D. S. Williams, H. Bregman, S. Knapp and E. Meggers, *Angew. Chem., Int. Ed.*, 2006, **45**, 1580–1585.

6 H. Qin, C. Zhao, Y. Sun, J. Ren and X. Qu, *J. Am. Chem. Soc.*, 2017, **139**, 16201–16209.

7 L. Xu, X. Wang, W. Wang, M. Sun, W. J. Choi, J.-Y. Kim, C. Hao, S. Li, A. Qu, M. Lu, X. Wu, F. M. Colombari, W. R. Gomes, A. L. Blanco, A. F. de Moura, X. Guo, H. Kuang, N. A. Kotov and C. Xu, *Nature*, 2022, **601**, 366–373.

8 M. M. Gottesman, T. Fojo and S. E. Bates, *Nat. Rev. Cancer*, 2002, **2**, 48–58.

9 A. Sharma, M.-G. Lee, H. Shi, M. Won, J. F. Arambula, J. L. Sessler, J. Y. Lee, S.-G. Chi and J. S. Kim, *Chem*, 2018, **4**, 2370–2383.

10 S. J. Dixon, K. M. Lemberg, M. R. Lamprecht, R. Skouta, E. M. Zaitsev, C. E. Gleason, D. N. Patel, A. J. Bauer, A. M. Cantley, W. S. Yang, B. Morrison III and B. R. Stockwell, *Cell*, 2012, **149**, 1060–1072.

11 C. Zhang, X. Liu, S. Jin, Y. Chen and R. Guo, *Mol. Cancer*, 2022, **21**, 47.

12 X. Jiang, B. R. Stockwell and M. Conrad, *Nat. Rev. Mol. Cell Biol.*, 2021, **22**, 266–282.

13 Y. Mou, J. Wang, J. Wu, D. He, C. Zhang, C. Duan and B. Li, *J. Hematol. Oncol.*, 2019, **12**, 34.

14 L. Zhao, X. Zhou, F. Xie, L. Zhang, H. Yan, J. Huang, C. Zhang, F. Zhou, J. Chen and L. Zhang, *Cancer Commun.*, 2022, **42**, 88–116.

15 G. Lei, L. Zhuang and B. Gan, *Nat. Rev. Cancer*, 2022, **22**, 381–396.

16 R. Birsen, C. Larrue, J. Decroocq, N. Johnson, N. Guiraud, M. Gotanegre, L. Cantero-Aguilar, E. Grignano, T. Huynh, M. Fontenay, O. Kosmider, P. Mayeux, N. Chapuis, J. E. Sarry, J. Tamburini and D. Bouscary, *Haematologica*, 2022, **107**, 403–416.

17 C. Bruedigam, A. H. Porter, A. Song, G. Vroeg In de Wei, T. Stoll, J. Straube, L. Cooper, G. Cheng, V. F. S. Kahl, A. P. Sobinoff, V. Y. Ling, B. M. C. Jebaraj, Y. Janardhanan, R. Haldar, L. J. Bray, L. Bullinger, F. H. Heidel, G. A. Kennedy, M. M. Hill, H. A. Pickett, O. Abdel-Wahab, G. Hartel and S. W. Lane, *Nat. Cancer*, 2024, **5**, 47–65.

18 M. A. Badgley, D. M. Kremer, H. C. Maurer, K. E. DelGiorno, H.-J. Lee, V. Purohit, I. R. Sagalovskiy, A. Ma, J. Kapilian, C. E. M. Firl, A. R. Decker, S. A. Sastra, C. F. Palermo, L. R. Andrade, P. Sajjakulnukit, L. Zhang, Z. P. Tolstyka, T. Hirschhorn, C. Lamb, T. Liu, W. Gu, E. S. Seeley, E. Stone, G. Georgiou, U. Manor, A. Iuga, G. M. Wahl, B. R. Stockwell, C. A. Lyssiotis and K. P. Olive, *Science*, 2020, **368**, 85–89.

19 X. Wang, F. Chen, J. Zhang, J. Sun, X. Zhao, Y. Zhu, W. Wei, J. Zhao and Z. Guo, *Sci. China: Chem.*, 2020, **63**, 65–72.

20 H. Yuan, Z. Han, Y. Chen, F. Qi, H. Fang, Z. Guo, S. Zhang and W. He, *Angew. Chem., Int. Ed.*, 2021, **60**, 8174–8181.

21 X. Zhao, J. Zhang, W. Zhang, Z. Guo, W. Wei, X. Wang and J. Zhao, *Chem. Sci.*, 2023, **14**, 1114–1122.

22 L. Wang, J. Karges, F. Wei, L. Xie, Z. Chen, G. Gasser, L. Ji and H. Chao, *Chem. Sci.*, 2023, **14**, 1461–1471.

23 X. He, L. Wei, J. Chen, S. Ge, M. Kandawa-Shultz, G. Shao and Y. Wang, *Inorg. Chem. Front.*, 2023, **10**, 4780–4788.

24 M. Shee, D. Zhang, M. Banerjee, S. Roy, B. Pal, A. Anoop, Y. Yuan and N. D. P. Singh, *Chem. Sci.*, 2023, **14**, 9872–9884.

25 W.-J. Wang, Y.-Y. Ling, Y.-M. Zhong, Z.-Y. Li, C.-P. Tan and Z.-W. Mao, *Angew. Chem., Int. Ed.*, 2022, **61**, e202115247.

26 Y.-Y. Ling, W.-J. Wang, L. Hao, X.-W. Wu, J.-H. Liang, H. Zhang, Z.-W. Mao and C.-P. Tan, *Small*, 2022, **18**, 2203659.

27 H. Zhao, M. Zhang, J. Zhang, Z. Sun, W. Zhang, W. Dong, C. Cheng, Y. Yao and K. Li, *Cell Biosci.*, 2023, **13**, 87.

28 W. Ma, W. Gao, Z. Ouyang, Y. Fan, H. Yu, M. Zhan, H. Wang, X. Shi and M. Shen, *Sci. China: Chem.*, 2022, **65**, 778–788.

29 J. Sagasser, B. N. Ma, D. Baecker, S. Salcher, M. Hermann, J. Lamprecht, S. Angerer, P. Obexer, B. Kircher and R. Gust, *J. Med. Chem.*, 2019, **62**, 8053–8061.

30 D. Baecker, B. N. Ma, J. Sagasser, L. Schultz, C. Hoerschlaeger, M. Weinreich, L. Steiner, B. Kircher and R. Gust, *Dalton Trans.*, 2020, **49**, 6842–6853.

31 L. Zhang, S. Ma, T. Wang, S. Li, L. Wang, D. Li, Y. Tian and Q. Zhang, *Anal. Chem.*, 2023, **95**, 1635–1642.

32 M. Hreusova, V. Novohradsky, L. Markova, H. Kostrhunova, I. Potocnak, V. Brabec and J. Kasparkova, *Bioinorg. Chem. Appl.*, 2022, **2022**, 3095749.

33 D. Romani, F. Marchetti, C. Di Nicola, M. Cuccioloni, C. Gong, A. M. Eleuteri, A. Galindo, F. Fadaei-Tirani, M. Nabissi and R. Pettinari, *J. Med. Chem.*, 2023, **66**, 3212–3225.

34 X.-X. Peng, H. Zhang, R. Zhang, Z.-H. Li, Z.-S. Yang, J. Zhang, S. Gao and J.-L. Zhang, *Angew. Chem., Int. Ed.*, 2023, **62**, e202307838.

35 X. Zheng, M. Liu, Y. Wu, Y. Chen, W. He and Z. Guo, *RSC Chem. Biol.*, 2024, **5**, 141–147.

36 S. Doll, F. P. Freitas, R. Shah, M. Aldrovandi, M. C. da Silva, I. Ingold, A. Goya Grocin, T. N. Xavier da Silva, E. Panzilius, C. H. Scheel, A. Mourão, K. Buday, M. Sato, J. Wanninger, T. Vignane, V. Mohana, M. Rehberg, A. Flatley, A. Schepers, A. Kurz, D. White, M. Sauer, M. Sattler, E. W. Tate, W. Schmitz, A. Schulze, V. O'Donnell, B. Proneth, G. M. Popowicz, D. A. Pratt, J. P. F. Angeli and M. Conrad, *Nature*, 2019, **575**, 693–698.

37 K. Bersuker, J. M. Hendricks, Z. Li, L. Magtanong, B. Ford, P. H. Tang, M. A. Roberts, B. Tong, T. J. Maimone, R. Zoncu, M. C. Bassik, D. K. Nomura, S. J. Dixon and J. A. Olzmann, *Nature*, 2019, **575**, 688–692.

38 T. Nakamura, C. Hipp, A. S. D. Mourao, J. Borggraefe, M. Aldrovandi, B. Henkelmann, J. Wanninger, E. Mishima, E. Lytton, D. Emler, B. Proneth, M. Sattler and M. Conrad, *Nature*, 2023, **619**, 371–377.

39 E. Marchi, R. Sinisi, G. Bergamini, M. Tragni, M. Monari, M. Bandini and P. Ceroni, *Chem.–Eur. J.*, 2012, **18**, 8765–8773.

40 J. Ma, X. Zhang, X. Huang, S. Luo and E. Meggers, *Nat. Protoc.*, 2018, **13**, 605–632.

41 M. Conrad, V. E. Kagan, H. Bayir, G. C. Pagnussat, B. Head, M. G. Traber and B. R. Stockwell, *Genes Dev.*, 2018, **32**, 602–619.

42 W. Zhang, M. Luo, B. Xiong and X. Liu, *J. Oncol.*, 2022, **2022**, 4000617.

43 A. Houessinon, C. François, C. Sauzay, C. Louandre, G. Mongelard, C. Godin, S. Bodeau, S. Takahashi, Z. Saidak, L. Gutierrez, J.-M. Régimbeau, N. Barget, J.-C. Barbare, N. Ganne, B. Chauffert, R. Coriat and A. Galmiche, *Mol. Cancer*, 2016, **15**, 38.

44 X. Sun, X. Niu, R. Chen, W. He, D. Chen, R. Kang and D. Tang, *Hepatology*, 2016, **64**, 488–500.

45 Y.-S. Ren, H.-L. Li, X.-H. Piao, Z.-Y. Yang, S.-M. Wang and Y.-W. Ge, *Biochem. Pharmacol.*, 2021, **194**, 114798.

46 S. Mozaffari-Jovin, T. Wandersleben, K. F. Santos, C. L. Will, R. Lührmann and M. C. Wahl, *Science*, 2013, **341**, 80–84.